Original Article

Influence of natural aging and ramping before artificial aging on the microstructure of two different 6xxx alloys

Christoph Martin Hell [a,], Hanne-Sofie Søreide [b], Ruben Bjørge [c], Calin Daniel Marioara [c], Yanjun Li [b], Randi Holmestad [a]*

[a] *Department of Physics, Norwegian University of Science and Technology (NTNU), Trondheim N-7491, Norway*
[b] *Department of Materials Science and Engineering, NTNU, Trondheim N-7491, Norway*
[c] *SINTEF Industry, Trondheim N-7465, Norway*

ARTICLE INFO

ABSTRACT

In this study the effect of a ramp up to artificial aging (AA) temperature in combination with natural aging (NA) was analyzed for two different industrial aluminium alloys. The alloys differ in their Mg/Si ratio as well as their copper (Cu) content. Both alloys have, however, a comparable amount of solute and dispersoid forming elements. The peak aged conditions of the alloys were investigated. NA prior to AA reduces the strength as compared with directly aged regardless of ramping. The hardness up to peak is very similar for conditions with and without the ramp if NA is performed, but for the Cu rich alloy a clear increase in peak hardness could be measured when ramped from the supersaturated solid solution (SSSS). The peak strength plateau is shorter for the ramped samples regardless of the NA time. Investigations by (scanning) transmission electron microscopy found longer but fewer precipitates when ramped from the SSSS and an increased precipitate number density when ramped after NA. Fewer hybrid-type precipitates and less overaged precipitates, e.g. B', and more L/C could be found for all ramped conditions. Atom probe tomography measurements showed that more solute is left in the matrix between the precipitates when ramped directly from the SSSS. This was related to a lower precipitate number density.

1. Introduction

Al–Mg–Si(-Cu) alloys, commonly referred to as the 6xxx series, are widely found in different applications of e.g. the automotive industry. Their high strength-to-weight ratio, relatively good weldability, formability and corrosion resistance make them an interesting candidate for replacing other heavier alloys [1].

Alloys of the 6xxx series are age hardened and receive their strength from the interaction of precipitates which are embedded in the matrix, with gliding dislocations [2]. The precipitates are constituted of the main alloying elements (Al, Mg, Si and Cu) and their formation is sensitively influenced by

the thermomechanical history of the alloy. By quenching from the solution heat treatment (SHT) temperature, one creates a precipitate-free supersaturated solid solution (SSSS) in which all of the alloying elements sit on Al lattice sites, creating substitutional point defects. Additionally, a high vacancy concentration gets trapped within the matrix. Keeping the SSSS at temperatures in which diffusion cannot be neglected, usually ≥ 0.3 homologous temperature, the point defects will group together and form new structures and eventually phases in the form of precipitates with the ultimate goal of successively lowering the systems free energy [3]. First, coherently embedded clusters are going to be formed in the SSSS and grow into larger, metastable and semi-coherently embedded precipitates [4]. Those will ultimately transform into the alloy's thermodynamic equilibrium phases which are usually incoherently embedded. During these transformations, the main growth and coherency direction of the metastable phases is parallel to the <100 > directions of the parental aluminum matrix [5]. As internally in the alloy the precipitates undergo changes of their number density, size, shape and composition; one can externally notice changes of the alloy's mechanical and physical properties. The typical precipitation sequence of Al–Mg–Si alloys is denoted as [6]:

$$SSSS \rightarrow Clusters \rightarrow GP-zones \rightarrow \beta'' \rightarrow \beta', B', U1, U2 \rightarrow \beta, Si$$
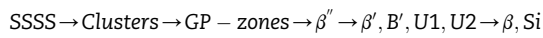
For Al–Mg–Si alloys that contain small amounts of Cu, the precipitation sequence is [5,7]:

$$SSSS \rightarrow Clusters \rightarrow GP-zones \rightarrow \beta'', L, C \rightarrow Q', \beta'_{Cu} \rightarrow Q, Si$$
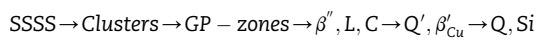
At peak strength, one finds a maximum amount of β'', L and some Q'/B' precipitates [8]. In overaged conditions of the 6xxx series, one will find that many of the β'' and L phases have dissolved or transformed into more mature phases that follow later in the precipitation sequence, e.g. Q' or B'. Quite often the observed precipitates constitute building blocks of different types of phases. Those phases are called hybrid precipitates [6,9].

A typical heat treatment for a 6xxx alloy consists of the SHT, the quench to room temperature (RT) and a subsequent artificial aging (AA) step at elevated temperatures, typically around 150 °C to 250 °C, to accelerate the precipitate formation [5]. During that process various parameters can influence the peak strength of 6xxx alloys. Milkereit et al. [10] reviewed the quench sensitivity and showed that a critical cooling rate is needed to suppress quench induced precipitation which can ultimately reduce the alloys age hardening potential. The 6xxx's temperature sensitivity can also be seen in its

characteristic so called "negative effect of natural aging" [4,11]: Keeping the SSSS of a dense alloy —typically an alloy with a solute content $\geq 1at.\%$— at RT prior to the AA step, referred to as natural aging (NA), one will see a later onset of the hardening response and a drop of peak strength relative to the directly aged (without NA) heat treatment [11]. Much effort has been put into understanding this. It is now commonly accepted that NA leads to the co-evolution of several types of competing clusters, some of which hinder the formation of precipitates in the following AA treatment [4,11,12]. Not much effort has yet been put into investigating the effect of ramping the alloy up to AA temperature. In this work we have selected two industrial common 6xxx alloys — AA6110 and AA6082 — and studied the effect of ramping to AA in combination with NA before AA. The alloys were chosen due to their different Mg/Si ratio and Cu content but otherwise relatively similar amount of dispersoid forming solute. The alloys were ramped to AA either directly after the water-quench —from the SSSS— or after 28 days of NA, hence from a clustered state.

Investigating the effect of a ramp to AA temperature does not just give us the possibility of comparing a typical industrial heating process to a heat treatment commonly conducted on lower laboratory scale. But it introduces the heating rate to AA temperature as a new parameter that can be worthy exploring. Due to their size or complex geometry, components produced in industry are usually subjected to the elevated AA temperatures at a slower pace, compared to the conventional small-scale samples in research laboratories. Yet in our experience, precipitate statistics acquired and fed into digital twins are often from samples that were submerged into preheated oilbaths, as an example one may look into the work from Myhr et al. [13]. Therefore we investigate the effect of a linear heating ramp to AA temperature on the hardness evolution, as well as precipitate type and size distribution on two different industrially relevant 6xxx Al alloys to study how a slower heating affects the microstructure and properties.

2. Methods and materials

2.1. Alloys and sample preparation

Extruded 6 mm thick profiles of the commercial alloys AA6110 and AA6082, in the following refererd to as 6110 and 6082, were water cut into $20 \times 35 \times 6$ mm rectangular samples. The alloys' compositions are given in Table 1. The samples were ground with a *Struers Rotopol 60* from 1200 grit SiC paper down

Table 1 – Alloy composition measured by optical emission spectroscopy and the range of chemical composition for the alloys 6110 and 6082 in at. % and wt.%. The range is given in wt. % in accordance to the AA standard.

	Si	Mg	Cu	Fe	Mn	Cr	Zn	Ti	Zr	V	B	Al
6110												
at. %	0.734	0.882	0.094	0.083	0.282	0.084	0.025	0.011	0.003	0.011	0.008	97.784
wt. %	0.760	0.790	0.220	0.170	0.570	0.160	0.060	0.020	0.010	0.020	0.003	97.217
	0.7–1.5	0.5–1.1	0.2–0.7	<0.8	0.2–0.7	0.04–0.25	<0.3	<0.15	–	–	–	–
6082												
at. %	0.878	0.725	0.004	0.102	0.257	0.083	0.025	0.011	–	0.011	0.010	97.894
wt. %	0.910	0.650	0.010	0.210	0.520	0.160	0.060	0.020	–	0.020	0.004	97.436
	0.7–1.3	0.6–1.2	<0.1	<0.5	0.4–1.0	<0.25	<0.2	<0.1	–	–	–	–

to 4000 grit SiC paper. The samples of the two alloys were solution heat treated for 45 min at 550 °C for the 6110 and 525 °C for the 6082. The SHT and the 0.02 $\frac{K}{sec}$ ramp to AA temperature were done in a *Nabertherm Forced Convection Chamber Furnace NA 15/65* and *Nabertherm Forced Convection Chamber Furnace NA 17/HR*, respectively. The furnaces were preheated, either to the SHT temperature or to RT.

Quenching was done directly into 25 °C ± 5 cold water. The AA was carried out at 175 °C ± 0.5 in a preheated *Memmert Oilbath*. The samples of the ramped treatments were transferred after the ramp simultaneously within < 10 s into the oilbath for further AA. Natural aging was done at RT for 28 days at 20.5 °C ± 0.5. Fig. 1 shows a schematic of the heat treatment and its inset displays the furnace and sample core temperature evolution during the ramp to AA. The core temperature was measured by inserting and centering a type K thermocouple with a 1.5 mm diameter into a 1.6 mm wide drilled channel and fixating it with a screw.

Resistivity and hardness measurements were carried out for all conditions after another grinding with 4000 SiC paper. 10 measurements were taken on individual samples per time step to follow the artificial aging response. The time steps were: 0 min, 10 min, 20 min, 40 min, 80 min, 160 min, 5 h, 10 h, 24 h, 3 d, 7 d. Micro hardness measurements were done with a dwell time of 10 s and a load of 1 kgf at an *Innovatest Vickers hardness testing machine* and the resistivity measurements with a *Sigmatest 2.069*. The measurements of the natural aging response were taken on one sample each for hardness and resistivity. Table 2 gives an overview of the different terms used to distinguish between the different heat-treatments in this study.

2.2. TEM sample preparation and (S)TEM setup

TEM samples were prepared by cutting normal to the extrusion direction and grinding down to 80 μm thin samples with a final grit of 4000, punching and electropolishing in a *Struers Tenupol-5* electropolishing unit. The electrolyte was a methanol: nitric acid (2:1) mixture. The parameters during the etching process were: 20 V, single flow, flow rate: 20, light stop: 60, Temperature: −25 °C ±8.

TEM investigations were carried out on a *Jeol JEM 2100* with a LaB6 cathode at an acceleration voltage of 200 keV and a condenser aperture of 70 μm. The HRTEM images were acquired with a 20 μm objetive lens aperture. The micrographs were recorded with a *Gatan 2k Orius CCD* camera. STEM investigations were carried out on a *Jeol JEM ARM200F*, double corrected (S)TEM with a cold field emission gun at 200 keV. A condenser aperture of 40 μm, corresponding to a semiconvergence angle of 27.42 mrad and a Gatan detector with inner and outer collection angle of 51−203 mrad for high-angle annular dark field (HAADF) recordings were chosen.

2.3. TEM image analysis

As the metastable precipitates are needles, rods or laths with elongation parallel to <100 > Al, TEM investigations were performed in grains with these orientations along the viewing direction. Due to specific grain texture in extruded materials,
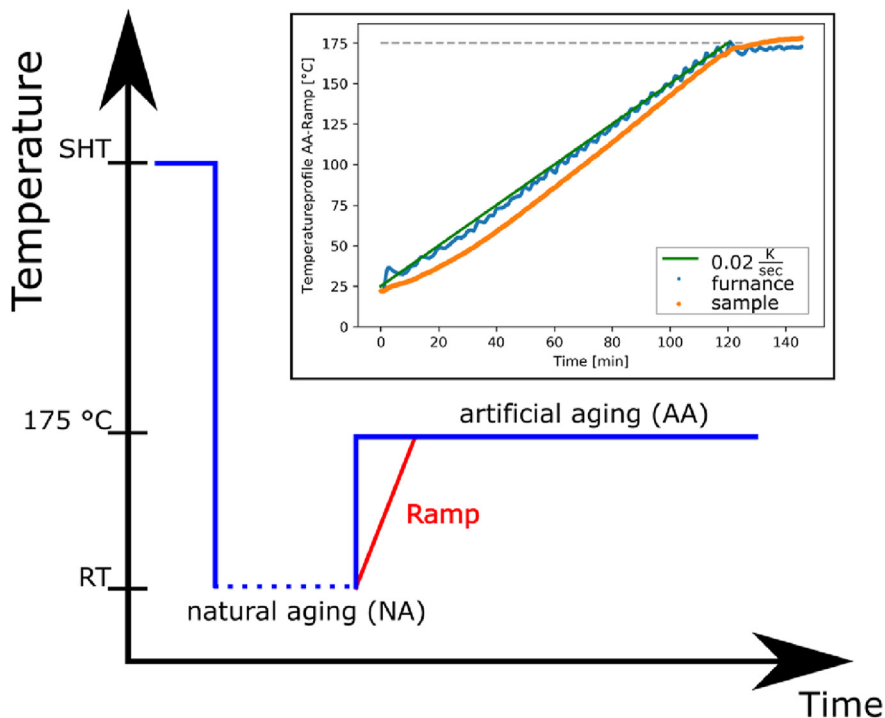

Fig. 1 — Schematic sketch of the heat treatment. The SHT temperature was 550 °C (6110) or 525 °C (6082) for 45 min. Some samples were naturally aged at RT for 28 days. Artificial aging treatment was conducted either in a pre-heated oilbath, or it started at RT and a 2 h linear ramp up to AA temperature preceded the isothermal age hardening process. The inset shows the ambient furnace temperature (blue) and the sample's core temperature (orange) during the linear ramp.

Table 2 — Used nomenclature to distinguish the 4 different heat-treatments.

Abbreviation	Explanation
DAA:	Direct Artificial Aging starts in preheated oilbath, ≤ 2 min natural aging at room temperature.
DrAA:	Direct Artificial Aging with a 0.02 $\frac{K}{sec}$ ramp starting in cold (RT) furnace.
NA + AA:	Natural Aging and Artificial Aging in preheated oilbath after 28 days storage at room temperature.
NA + rAA:	Natural Aging and Artificial Aging with a 0.02 $\frac{K}{sec}$ ramp from RT after 28 days storage at room temperature.

such grains are most likely to be found along the extrusion direction, which was chosen as viewing direction. The TEM precipitate statistics quantification builds on [14]. For each condition a set of bright field (BF), dark field (DF), convergent-beam electron diffraction (CBED) and high-resolution TEM (HRTEM) micrographs were taken in the [001] zone axis of Al. The mean precipitate length l_{mean} was determined by measuring $\sim$ 400 precipitates from different BF images. The thickness t of the same areas was measured through 2-beam CBED by tilting slightly off zone [15]. The number density was determined by counting N precipitates per area from DF images and the corrected number density ρ per DF was determined as the average from up to 5 areas, each determined through [14]:

$$\rho = \frac{3N}{At\left(1 + \frac{l_{mean}}{t}\right)} \qquad (1)$$

Through fitting rectangles to $\sim$ 200 precipitate cross sections (CS) from HRTEM micrographs, the average CS was found. Deviations from the mean are expressed through the standard error for the CS and the standard deviation for ρ and l_{mean}.

2.4. APT sample preparation and acquisition

Samples from the DrAA and DAA treatments of both alloys were prepared for analysis by atom probe tomography (APT). The samples were cut into small rods and ground on SiC paper to the dimensions 20 × 0.4 × 0.4 mm. A two-step manual electropolishing method was carried out at room temperature with a horizontal micro-loop setup [16]. A solution of 25 vol% perchloric acid in glacial acetic acid was used as electrolyte in the first step. 10 vol% perchloric acid in glacial acetic acid, as well as, 2 vol% perchloric acid in 2-butoxyethanol solutions were used in the second, needle-sharpening step. A polishing voltage of $\sim$ 20 V_{dc} and 4–12 V_{dc} was applied in the first and second step, respectively.

The APT experiments were carried out with a laser-assisted *Local Electrode Atom Probe, LEAP 5000XS*, from CAMECA. The analyses were performed in laser mode at a temperature of 30 K and pressure below 3.0×10^{-9} Pa. The energy of the applied laser pulses was calibrated for each

individual analysis to yield an equivalent pulse fraction of 25% [17]. The pulse frequency was kept at 250 kHz, and the standing voltage during the analysis was automatically adjusted by the instrument in order to maintain a detection rate of 0.005 evaporation events per laser pulse. 25 million ions were collected during the APT acquisitions for 6110 DAA and 44 million for 6110 DrAA. Datasets consisting of 13 million and 15 million ions were analyzed for alloy 6082 DAA and DrAA.

2.5. APT data analysis

The software *AP Suite*^{TM} 6.1 was used for the reconstruction and analysis of the APT data. A differentiation is made between atoms belonging to the *bulk* and to the *matrix* of the data. The bulk covers every atom in the volume, while the matrix is the volume between the precipitated phases, as visualized in Fig. 2. The bulk composition is the composition of the total analyzed volume by APT including both the precipitates and the matrix surrounding them. The matrix atoms belong to the volume between the precipitates and were extracted by the use of iso-concentration surfaces. Due to trajectory aberrations caused by a difference in evaporation fields between the matrix and precipitate phases, the precipitates in 6xxx alloys typically appear dilated in the APT data, and their interface with the matrix is not sharp [18,19]. The thresholds of the iso-concentration surfaces were, thus, selected as a compromise between maximizing the matrix volume for further analysis while excluding both the precipitates and their diffuse interface
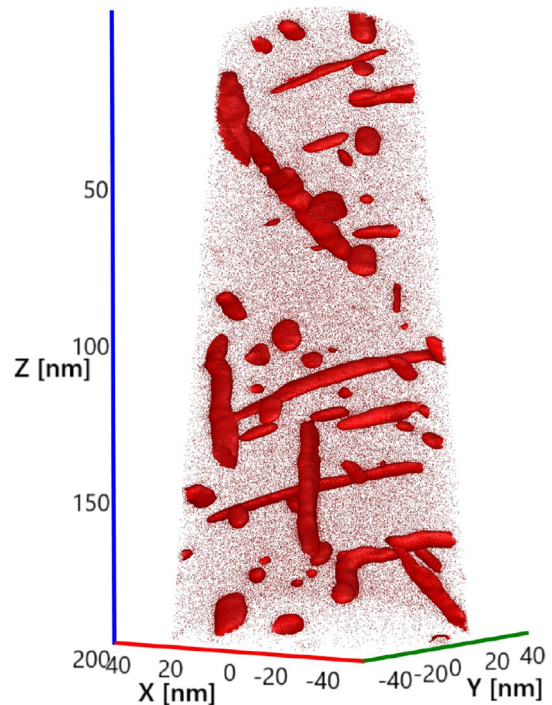

Fig. 2 — Reconstructed bulk volume of 6110 DrAA displaying the microstructure at peak hardness. Iso-concentration surfaces are drawn at a threshold of 11 at.% Mg + Si to emphasize the precipitates. All the atoms recorded are referred to as *bulk atoms*. The atoms not part of the precipitates, are referred to as *matrix atoms*.

with the adjacent matrix. Concentration profiles were additionally applied to confirm the selected thresholds.

3. Results

In this section the results of the hardness and conductivity evolution during NA and AA are presented. The precipitate statistics from TEM, as described above, is presented as well as the precipitate-type analysis for the eight different conditions. At the end of this chapter, the results from the APT analysis are given.

3.1. Hardness and conductivity measurements

3.1.1. Change of hardness and conductivity during natural aging

Fig. 3 shows the hardness and conductivity response for the two alloys during NA. The hardness evolution during NA shows for both alloys an initial stage which develops into a rapid hardening stage after roughly 20 min [12]. During the initial stage not much change in hardness can be detected. 6082 shows after roughly 300 min a transition into a slow hardening regime. 6110, however, is still in the rapid hardening stage after the same amount of NA time. The transition from rapid hardening to slow hardening occurs roughly after 25 h. The 6082 alloy seems to show an additional stage after roughly 1 month of NA where the hardening kinetics flatten out.

The conductivity curve shows a qualitatively similar but opposite behaviour. The onset of clustering, seen by a decrease in conductivity, seems to start later in the 6110 alloy. One could argue that there is no apparent initial stage in the conductivity plot of the 6082 since the conductivity already changed by 0.1 $\frac{MS}{m}$ within the first 10 min. The onset of the rapid stage in the conductivity plot looks similar for both alloys and is taken as a reference for the end of the initial stage. The rapid stage of conductivity change can be seen to occur for the 6082 after 10 min of NA. The 6110 alloy shows the onset

of the rapid stage after roughly 30 min NA. Even though the rapid stage starts later in the 6110 it lasts much longer, for nearly 270 min. The rapid stage of the 6082 seems to have transitioned into the slow stage after roughly 70 min.

3.1.2. Hardness and electrical conductivity evolution during artificial aging

Fig. 4 displays the hardness and electrical conductivity evolution of the two alloys during AA for the DAA (blue, solid) and NA + AA (blue, dashed) and DrAA (red, solid) and NA + rAA (red, dashed) heat treatments. In the 6110 alloy, see Fig. 4 (a) and (c), the DrAA treatment slows down the AA hardening kinetics compared to the DAA treatment but increases the peak hardness value. The NA + AA and NA + rAA treatments of 6110 lead to a delayed AA response and a lower overall hardness. The hardness plateau is shorter for both heat treatments with a ramp compared to no ramp. The conductivity curves of the different heat treatments show little changes within the first 20 min of AA. However, heat treatments which were subjected to 28 days of NA showed a substantially lower initial conductivity value compared to the conditions without NA. After 20 min AA an explosive increase in conductivity is seen for the DAA treatment. The conductivity curve of the NA + AA treatment shows a change in conductivity which follows after 20 min AA a linear appearing change in the semi-logarithmic plot. The two ramped heat treatments (DrAA and NA + rAA) show a course which is qualitatively similar to the one of the NA + AA treatment. In the overaged regime after around one day of AA, all the curves seem to follow a similar growth behaviour.

The hardness and conductivity curves for the 6082 alloy can be seen in Fig. 4 (b) and (d). In general, 6082 shows a lower hardness compared to 6110, but a higher conductivity. For the 6082, the DrAA treatment does not result in a higher peak hardness value, nor does it delay the AA response when comparing to the DAA treatment. The thermal stability of the hardness for the ramped heat treatments is reduced, as well. Furthermore, the double peak which is sometimes encountered in 6xxx type alloys, disappeared when ramped. The
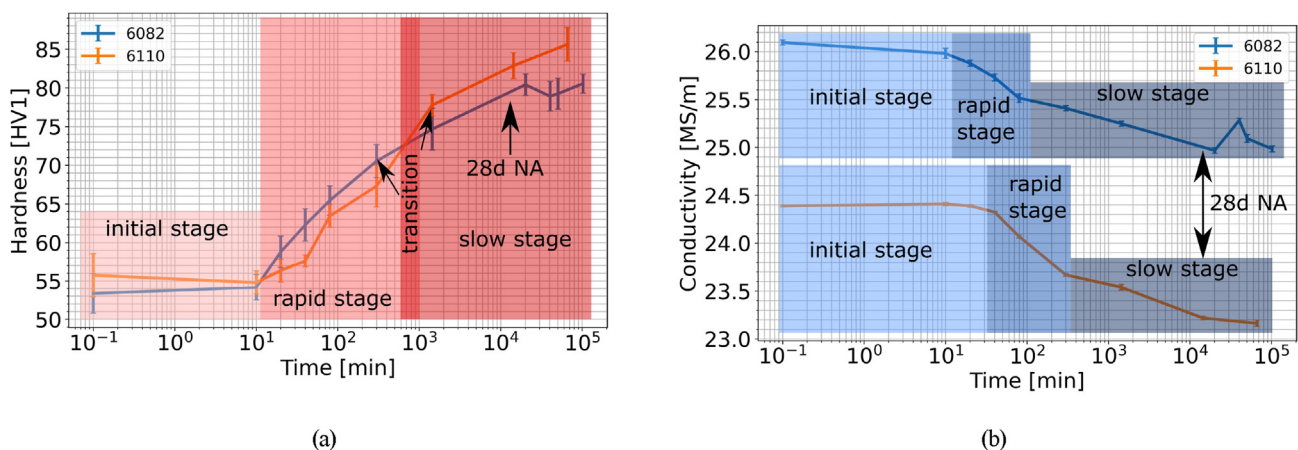

(a)   (b)

Fig. 3 − (a) Hardness curves and (b) Conductivity curves of the 6082 and 6110 during NA. The different stages of the hardness and conductivity evolution during NA, as introduced by Banhart et al. [12] are indicated. Note that the names of the stages are just a description of the hardness/conductivity evolution and do not necessarily correspond to the same time stamps in the two plots.
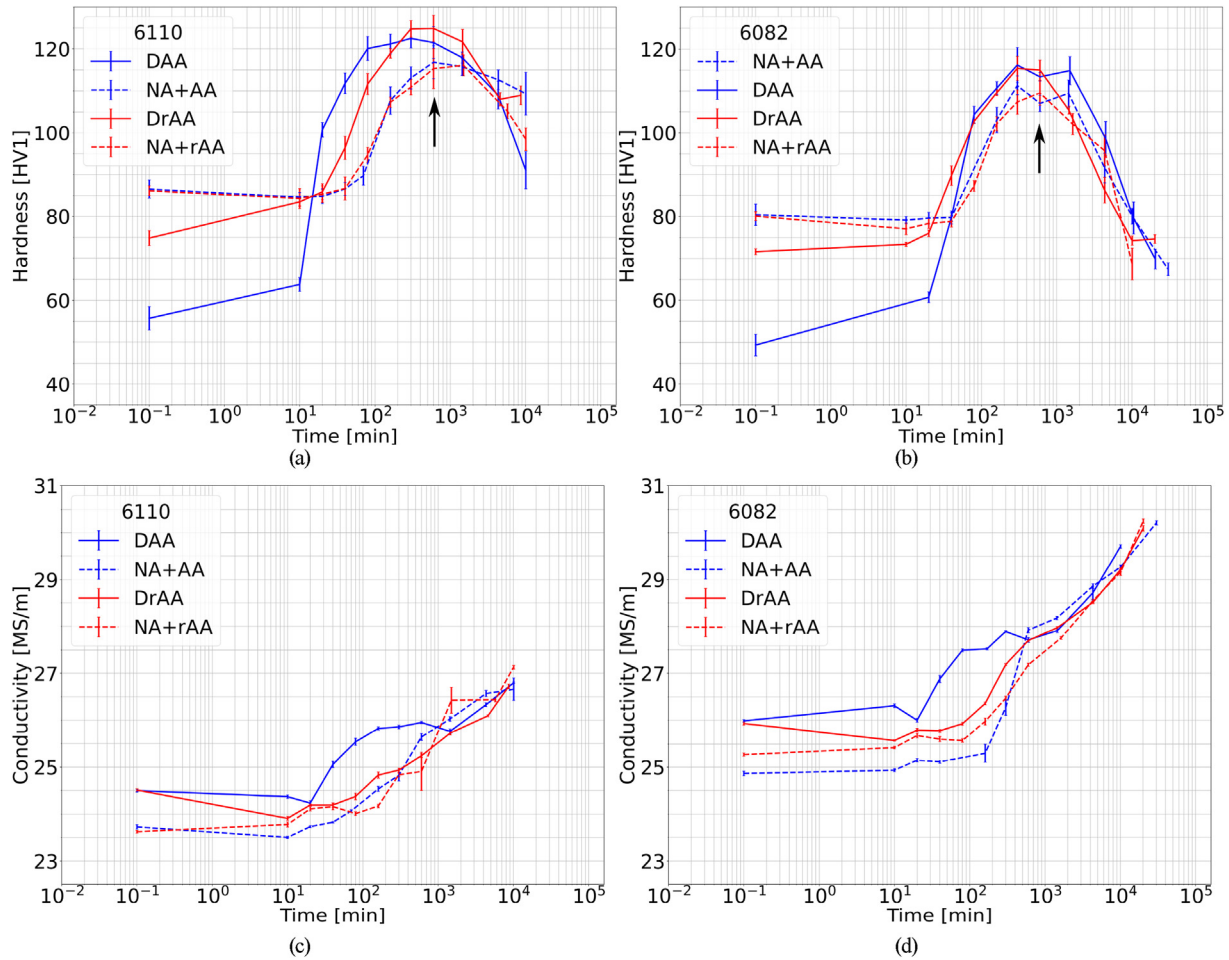
Fig. 4 — Hardness and conductivity curves of the AA response at 175 °C for (a), (c) 6110 and (b), (d) 6082. The first measurements of the DAA and NA + AA treatments were taken right before the AA treatment and relate to either the as quenched condition (blue solid line) or the 28d naturally aged condition (blue dashed line). The first measurements of the ramped curves (red) were taken right after the 2 h linear ramp finished and before the isothermal heat treatment started. The dark arrows in the hardness curves mark the conditions corresponding to 10 h isothermal AA that are near peak hardness and were chosen for further (S)TEM and APT investigations.

conductivity curves show a similar trend as the ones of the 6110. The conditions with NA prior to AA showed for the 6082 a lower initial conductivity value. The DAA treatment shows a strong logarithmic growth behaviour after around 20 min AA in the semi-logarithmic plot, comparable to the one observed in the 6110. The NA + AA heat treatment results in a delayed exponentially appearing increase of change after 20 min of AA. The two ramped conditions show a higher similarity in the change of conductivity with the NA + AA heat treatment. During the overaged regime after around one day of AA, the four heat treatments follow a similar trend which appears linear in the semi-logarithmic plot.

3.2. Precipitate statistics studied by TEM

The TEM precipitation analysis were conducted on the 4 conditions per alloy after 10 h isothermal AA at 175 °C.

3.2.1. 6110

Fig. 5 shows examples of bright field (BF) and dark field (DF) micrographs of the peak hardness conditions and the measured precipitate size distributions. Table 3 summarizes the results of the TEM analysis for this alloy. The following observations can be drawn:

- 28 days NA reduced precipitate number density but increased precipitate size regardless of ramping.
- The ramp reduced precipitate number density for the direct aging case while increasing it slightly after 28 days NA.
- DrAA shows an increased precipitate aspect ratio $\left(\frac{l_{mean}}{\sqrt{CS}}\right)$ compared to DAA. This is not seen as drastically for the NA + AA and NA + rAA cases.
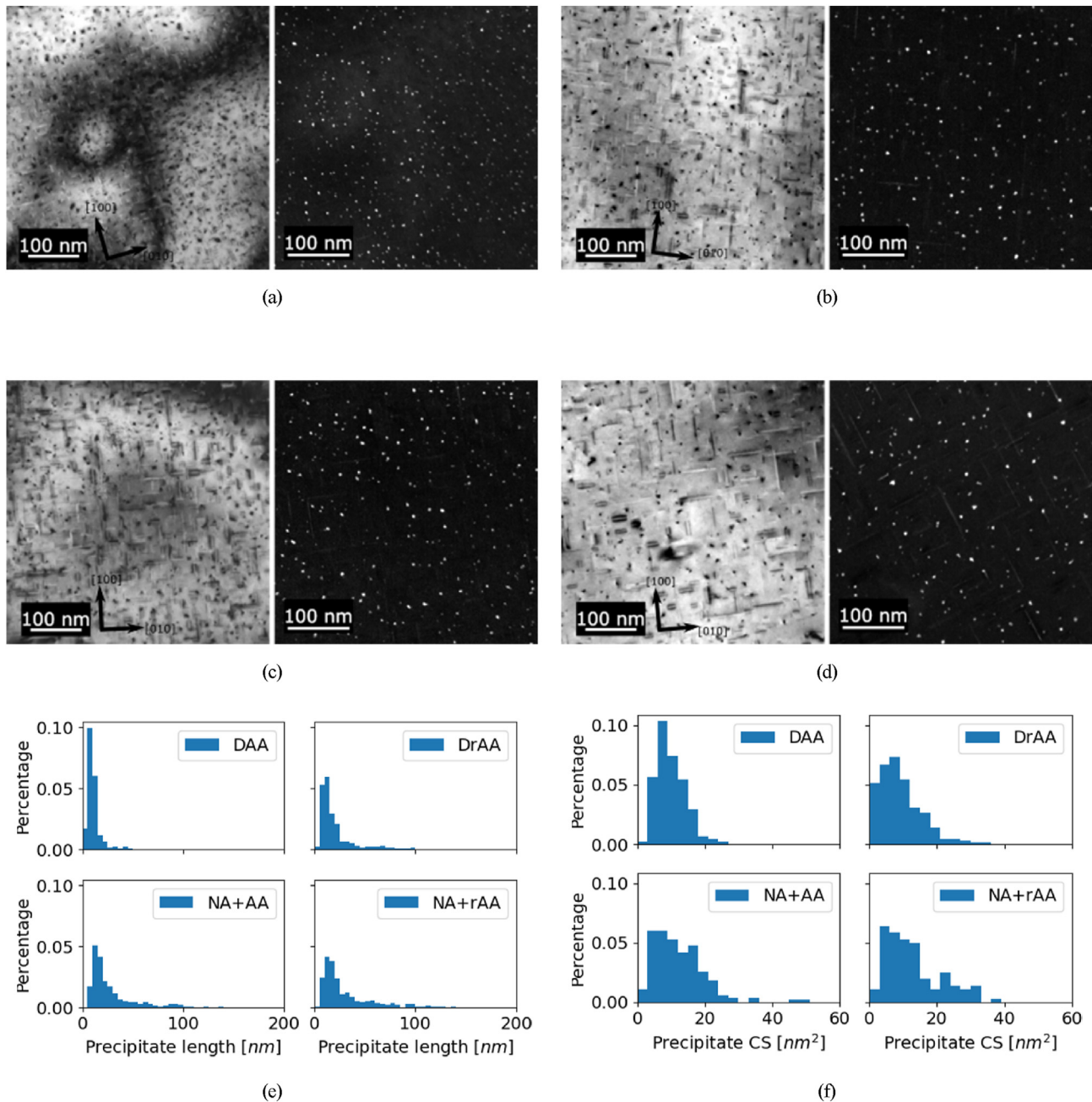
(a)

(b)

(c)

(d)

(e)

(f)

Fig. 5 — Example BF and corresponding DF micrographs for the 4 conditions investigated of the 6110 alloy and the thickness t of the portrayed images. (a) DAA, t: 58.5 nm; (b) DrAA, t: 52.7 nm; (c) NA + AA, t: 76.2 nm; (d) NA + rAA, t: 44.1 nm. All samples had 10 h of isothermal annealing at 175 °C. The <100 > directions are indicated. (e) Normalized histograms of the measured needle length with a binwidth of 5; (f) Normalized histograms of the measured CS with a binwidth of 3.

Table 3 — Summary of the precipitate statistics for alloy 6110 after 10 h isothermal AA at 175 °C.				
	AA from SSSS		AA after NA	
	DAA	DrAA	NA + AA	NA + rAA
Average needle length [nm]	10.6 ± 0.5	19.0 ± 0.8	27.0 ± 1.2	28.9 ± 1.2
Average CS [nm^2]	9.9 ± 0.4	9.1 ± 0.4	12.3 ± 0.6	12.8 ± 0.7
Precipitate aspect ratio	3.4	6.3	7.7	8.1
Average number density $[\frac{\#}{\mu m^3}]$	$(133 \pm 16.8)x10^3$	$(85 \pm 18.8)x10^3$	$(51 \pm 9.2)x10^3$	$(64 \pm 2.2)x10^3$

3.2.2. 6082

Fig. 6 shows BF and DF micrographs from the 6082 alloy for the analyzed 10 h AA at 175 °C conditions and the measured precipitate size distributions. Table 4 summarizes the results of the TEM analysis of the 6082 alloy. The following observations can be drawn:

- 28 days NA decreased the precipitate number density and increased the precipitate CS if not ramped.

- The ramp increased the precipitate number density and lowered the precipitate CS after NA.
- The ramp decreased ρ and increased the average precipitate length when directly aged but lowered the average length for ramping after NA.

3.3. Precipitate types studied by HAADF-STEM

The precipitate types were analyzed on the basis of several HAADF micrographs of precipitate CS taken in the bulk of a
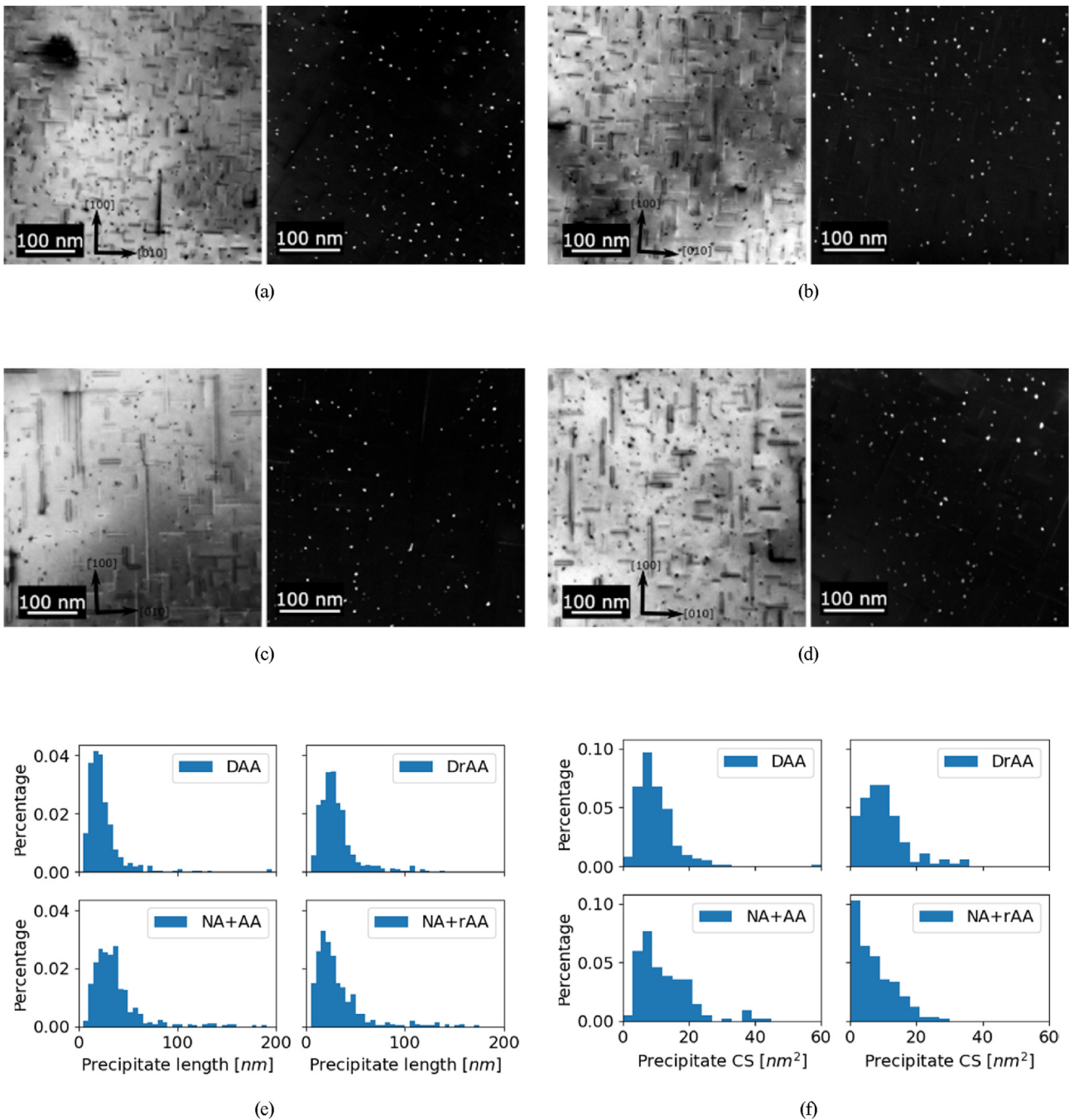

Fig. 6 — Example BF and corresponding DF micrographs for the 4 conditions investigated of the 6082 alloy and the thickness t of the portrayed images. (a) DAA, t: 40.3 nm; (b) DrAA, t: 44.5 nm; (c) NA + AA, t: 50.9 nm and (d) NA + rAA, t: 43.5 nm. All samples had 10 h isothermal AA at 175 °C. The <100 > directions are indicated. (e) Normalized histograms of the measured needle length with a binwidth of 5; (f) Normalized histograms of the measured CS with a binwidth of 3.

Table 4 – Summary of the precipitate statistics for alloy 6082 after 10 h isothermal AA at 175 °C.

	AA from SSSS		AA after NA	
	DAA	DrAA	NA + AA	NA + rAA
Average needle length [nm]	25.0 ± 1.1	31.0 ± 1.4	39.2 ± 1.7	31.1 ± 1.7
Average CS [nm^2]	10.2 ± 0.4	9.8 ± 0.5	12.7 ± 0.7	7.5 ± 0.4
Precipitate aspect ratio	7.8	9.9	11.0	11.4
Average number density $[\frac{\#}{\mu m^3}]$	$(63 \pm 5.5)x10^3$	$(52 \pm 3.9)x10^3$	$(39 \pm 1.2)x10^3$	$(65 \pm 4.4)x10^3$

grain. Precipitates that grew on dislocations or dispersoids were omitted. The images of those precipitate CS were categorized into five different groups based on the occurrence of typical building blocks of different phases and phase-typical morphologies:

1. $\beta''_{perfect}$: Perfect β''-type precipitates contain only the "eye"-like β''-building block [5]. Structural imperfections, like the visible incorporation of Cu or stacking faults were tolerated. In the example images of $\beta''_{perfect}$ and β''_{Hybrid} in Figs. 7 and 8 the typical β''-eye is highlighted.
2. β''_{Hybrid}: Hybrid β''-type precipitates show a large continuous region of β'', but other phases, e.g. U2 or Q' were structurally incorporated into the precipitate CS. In the example image of a β''_{Hybrid} from Fig. 7, the Q' building block is highlighted besides the β''-eye.
3. L/C: The <100 > oriented precipitates of the hybrid L-type or ordered C-type [7].
4. Q'/B': Precipitates showing structures of the isostructural Q' and B' phases, as seen in Figs. 7 and 8.
5. Hybrid/post-β'': Phases that did not fit into one of the other categories. Typically overaged phases, e.g. β', U2, or hybrid phases without a dominating sub-structure.

To avoid searching biased for precipitates, e.g. by the strong contrast of Cu-rich precipitates, the magnification was always kept at 10 M × or higher while searching through the grains. Table 5 and Table 6 display the occurrence and the amount of measured precipitates for the two alloys and the different heat treatments. The main occurring precipitate after 10 h AA was of the β''-type for all conditions. However, it can be seen that ramping and NA influenced the relative occurrence of the different precipitate types.

NA for 28 days increased the amount of hybrid phases and post-β'' in both alloys. For the Cu-rich 6110, ramping led to an increase of the L/C phase, as well as a reduction of β''_{hybrid}. For the 6082 a slight increase of B' phases was found when no ramp was applied. The ramp, on the other hand, led to the increase of $\beta''_{perfect}$. Figs. 7 and 8 display example precipitates of each of the categories found in the two alloys.

3.4. APT analysis

The concentration of solute in bulk after 10 h isothermal AA treatment for DAA and DrAA is presented in Table 7 for 6110 and Table 8 for 6082. Some deviations in the measured compositions from the given alloy compositions are expected. APT measurements are done on a small volume of the material and provides insight into the local microstructure and chemical composition of that volume. A surplus of Cu can be linked to re-deposition of Cu during sample preparation by electropolishing [20]. Furthermore, a portion of Si has already been consumed by primary particles and dispersoids [21].

The tables display three columns for each condition. The *bulk composition* is the overall composition of Mg, Si and Cu measured in the full dataset. The *matrix composition* is that of Mg, Si and Cu in regions outside of the precipitates. The column named *solid solution* represents the amount of solute remaining in the matrix, and is given as the ratio of the matrix concentration to the bulk concentration of each element. The higher the value given in this column, the larger is the amount of the total solute content still in solid solution at the analyzed peak hardened conditions.

3.4.1. 6110
For the Cu-containing Mg-rich 6110, a clear difference between the DAA and DrAA heat treatments can be seen in the APT data. Iso-concentration surfaces set at a threshold of 1.3 at.% Mg were used to extract the matrix volume between the precipitates. The measured matrix composition of DAA and DrAA were compared to their respective measured bulk composition, to calculate the degree of solute depletion between the precipitates. The amount of solute left in the matrix between the precipitates is significantly higher for the DrAA compared to DAA. The Mg and Si content of 6110 DrAA is about two and three times higher than for the 6110 DAA. The largest standard deviation of the statistical error of the measured bulk and matrix solute compositions is below 0.003 at.%.

3.4.2. 6082
The matrix of 6082 DAA and 6082 DrAA was extracted by removing the precipitates defined by iso-concentration surfaces drawn at 0.35 at.% Mg. The solute remaining in the

Table 5 – Summary of the precipitate type statistics for alloy 6110. Percentages may not total 100% due to rounding.

	$\beta''_{perfect}$	β''_{hybrid}	L/C	Q'/B'	Hybrid/post-β''	Measured precipitates
DAA	48.6%	35.1%	2.7%	–	13.5%	37
DrAA	43.8%	18.8%	25%	–	12.5%	17
NA + AA	16.8%	28.6%	23.4%	–	31.2%	77
NA + rAA	20.7%	12.1%	36.2%	–	31%	58

Table 6 — Summary of the precipitate type statistics for alloy 6082. Percentages may not total 100% due to rounding.

	$\beta''_{perfect}$	β''_{hybrid}	L/C	Q'/B'	Hybrid/post-β''	Measured precipitates
DAA	53.1%	25%	6.3%	9.4%	6.3%	32
DrAA	80.8%	7.7%	—	3.8%	7.7%	26
NA + AA	35%	17.5%	5%	10%	32.5%	40
NA + rAA	51.2%	25.6%	4.7%	4.7%	14%	43

matrix showed no significant difference between DAA and DrAA treatments for this alloy. The amount of Mg and Si still dissolved between the precipitates was close to 10% and 30%, respectively, for both DAA and DrAA. The largest standard deviation of the statistical error of the measured bulk and matrix compositions in Table 8 was 0.005 at.%.

4.   Discussion

4.1.   The effect of clustering on the peak strength microstructure

Esmaeili et al. [22] suggested that the decomposition of Al—Mg—Si(-Cu) alloys' as-quenched SSSS is a two-stage process which can be followed by tracking the change of hardness and conductivity during NA, refer to Fig. 3. The 28 days of NA disintegrated the SSSS substantially which can be seen by the increase of hardness by roughly 30 HV or the decrease of
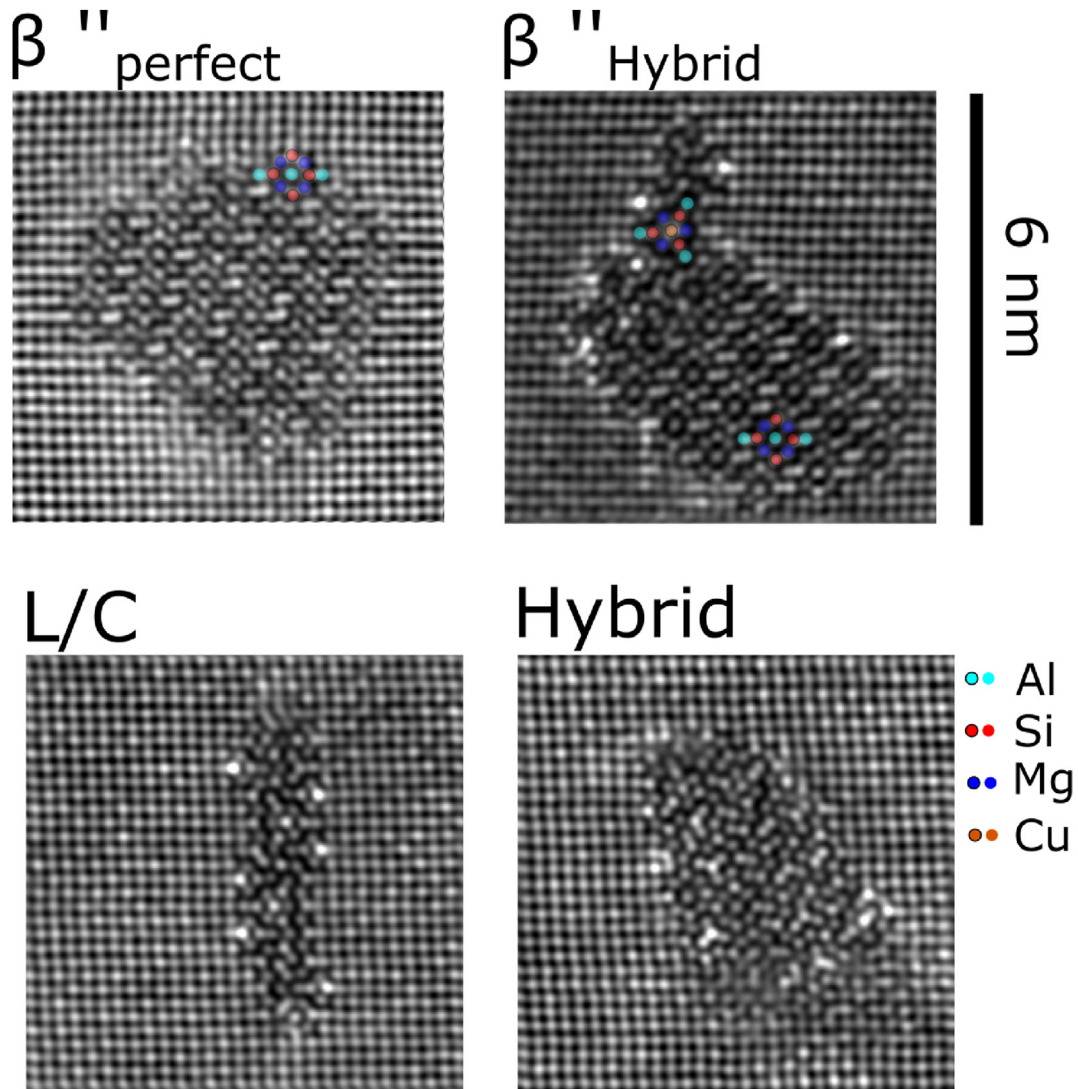

Fig. 7 — Examples of the different precipitate categories in 6110. The micrographs were Fourier-filtered with a cut-off radius of ~6 nm^{-1} and share the same scale bar. The precipitates displayed were found in the DAA 6110 sample ($\beta''_{perfect}$) and the NA + rAA 6110 sample (β''_{hybrid}, L, Hybrid). Atomic overlays of the Q' and β'' building blocks are indicated.
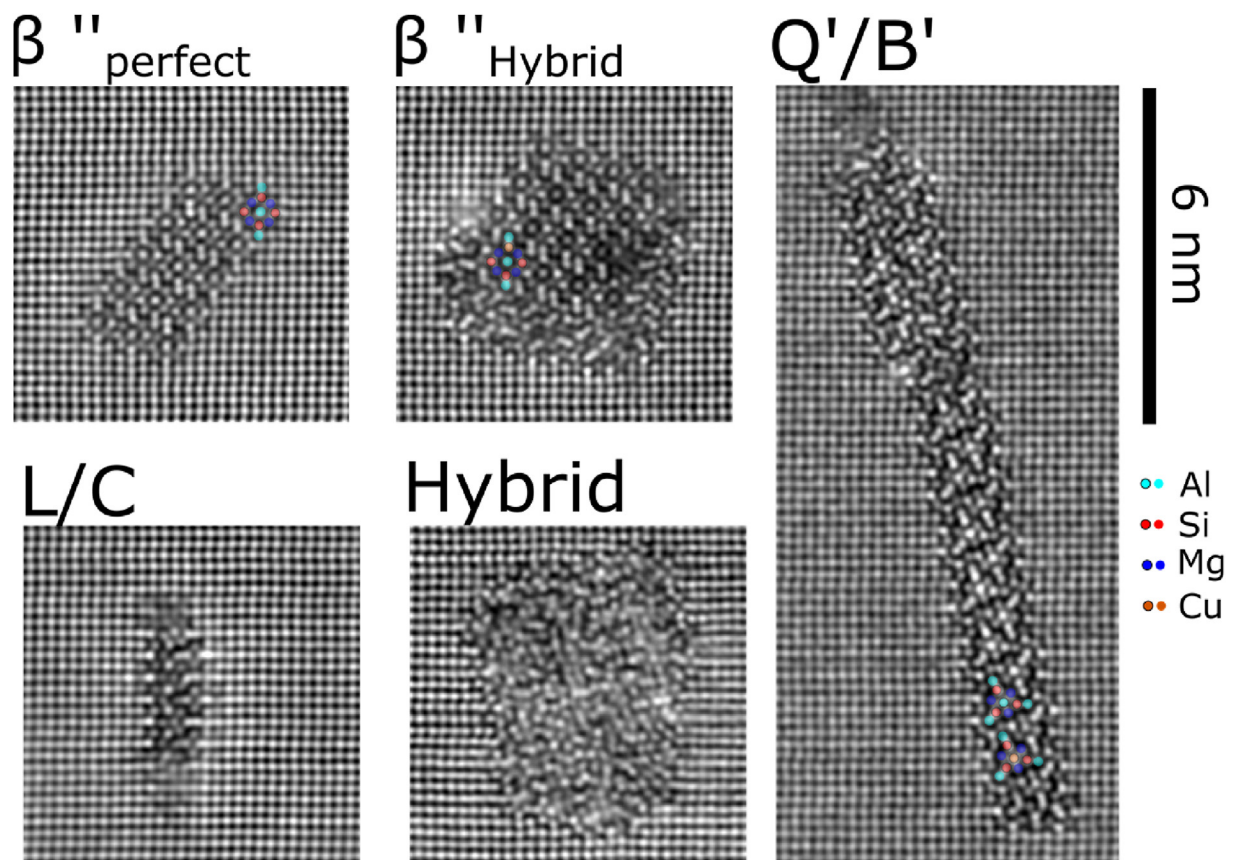
Fig. 8 − **Examples of the different precipitate categories in 6082. The micrographs were Fourier-filtered with a cut-off radius of ~6 nm^{-1} and share the same scale bar. The precipitates displayed were found in the DAA 6082 sample ($\beta''_{perfect}$, β''_{hybrid}, C, B′) and the NA + AA 6082 sample (*Hybrid*). Atomic overlays of the Q′, B′, β'' and β''_{hybrid} structures are indicated.**

conductivity by ~ 1 MS/m, for both alloys compared to their as-quenched values. She associated the changes during the initial stage and rapid stage to so-called *quenching clusters* while the further decomposition and change of hardness and conductivity during the slow stage was related to *NA clusters*. It is not much known about the clusters which form during NA. The combined results of different analysis methods indicate that during NA clusters of different stoichiometry evolve [11,12,23,24]. A sequence was, however, not found since contradicting results were found and APTs are running at their detection and sensibility limit due to the small size and similarity of the clusters [4]. The majority of results lets assume that first mono-clusters evolve, which later on incorporate other elements and develop into co-clusters. The formation of Si−Si mono-clusters can be assumed to happen early on, due to Si's low solubility in Al and its high diffusivity. Those Si−Si mono-clusters start to incorporate Mg at later stages of NA and transform into Mg−Si co-clusters of different stoichiometry [12,23−25]. Peng et al. [26] showed from first-principles calculations that vacancies can be incorporated into those different clusters, e.g. Si−Si and Cu−Cu mono-clusters or Mg−Si and Mg−Cu co-clusters, during NA. This incorporation of vacancies can decelerate the NA kinetics, and could cause the transition into the slow stage of hardening or conductivity change, as seen in Fig. 3 (a) and (b). When

Table 7 − **Concentration of the solutes Mg, Si and Cu measured by APT for DAA and DrAA 6110 in bulk and in matrix as well as the amount of solute preserved in solid solution.**

at.%	DAA			DrAA		
	Bulk	Matrix	Solid solution	Bulk	Matrix	Solid solution
Mg	0.90	0.25	27.9%	0.86	0.49	56.5%
Si	0.41	0.08	19.7%	0.49	0.30	61.1%
Cu	0.19	0.10	51.6%	0.12	0.09	74.8%

Table 8 − **Concentration of the solutes Mg and Si measured by APT for DAA and DrAA treated 6082 in bulk and in matrix as well as the amount of solute preserved in solid solution.**

at.%	DAA			DrAA		
	Bulk	Matrix	Solid solution	Bulk	Matrix	Solid solution
Mg	0.77	0.06	8.4%	0.73	0.07	9.2%
Si	0.53	0.16	30.9%	0.52	0.16	31.2%

exposing the clustered SSSS to AA temperatures, a slight softening due to the dissolution of some clusters, called retrogression, can be observed, see Fig. 4 (a) and (b). The negative effect of clustering in dense alloys of the 6xxx family is then the combined interplay of many different effects connected to the early clusters. Ultimately, heat treatments with NA prior to AA result in an increased material hardness at the beginning of AA due to the presence of clusters, a later onset of hardness increase during AA due to retrogression and a reduced peak strength due to a coarser microstructure [11,27].

The negative effect can be seen in this study by comparing the DAA treatments, for which the RT storage was minimal, to the NA + AA treatments. The clusters which formed during NA lead to a coarser precipitate microstructure. The l_{mean} and CS is larger for the NA + AA heat treatment which correlates with the findings of more Hybrid/post-β"-type phases. Furthermore, the average precipitate number density is reduced after 28 days of NA. In the conductivity curves from Fig. 4 (c) and (d) a strong increase in conductivity after about 20 min AA was measured during the DAA treatment, which relates to the sudden nucleation and growth of many precipitates. The reason for a coarser microstructure after RT storage is not known and different explanations exist. Pogatscher et al. [28,29] link the formation of less precipitates to a reduction of freely available vacancies and solute since clusters are already binding them (vacancy-prison mechanism). Following Tao's et al. [30] explanation, the commonly observed reduced precipitate number density after NA is due to heterogeneous nucleation of precipitates on few thermally resistant clusters. Those clusters act as heterogeneous nucleation sites during the initial stages of AA. The remaining solute in the SSSS would thus migrate to those persistent clusters, on which the precipitates can easier form. This heterogeneous nucleation will result in an overall reduced precipitate number density, compared to the homogeneous nucleation of precipitates freely within the Al matrix. The small drop in hardness in Fig. 4 (a) and (b) for the NA + AA (and NA + rAA) treatments due to the dissolution of clusters suggest that many of the clusters do still exist when the precipitates starts to grow and noticeably change the hardness. This supports the theory of heterogeneous nucleation by Tao et al. [30]. For both alloys we observe more of the overaged and hybrid phases after NA, regardless of ramp, as seen in Tables 5 and 6. This can be explained in two ways: (i) by release of more vacancies and solutes during the retrogression [28] or (ii) by accelerated precipitation kinetics due to reduction of phase transformation barriers by heterogeneous nucleation [30]. The increased occurrence of overaged and hybrid phases appears in the TEM data as an increased average CS, see Tables 3 and 4.

4.2. The effect of a ramp and Cu on clusters

When comparing the average precipitate number density of the NA + AA to the NA + rAA treatment, one notices that the latter is increased for both alloys. Hence, the ramp stimulated the formation of fruitful precipitate nucleation sites, which is in good agreement with the findings by Shi et al. [31]. Shi hypothesized a critical heat-up rate to AA above which clusters show the tendency to dissolve. Ramping less steep however,

stimulates cluster formation and thus precipitation. They found the critical rate to be around $0.09 \frac{K}{sec}$. The ramp applied in this work lies roughly at $0.02 \frac{K}{sec}$, hence lower than the proposed critical value. It is quite apparent that the precipitate number density of 6082 is more severely affected by the ramp, compared to 6110, which is due to Cu in 6110. The NA curves from Fig. 3 show, as well, that more changes happen during the RT storage in the 6082 compared to the 6110, e.g. the earlier onset of the rapid stage. Zandbergen et al. [32] demonstrated that during NA only for alloys containing a minimum of 0.06 at.% Cu, the amount of Cu in the clusters increases after a week of NA. The incorporation of intermediate sized Cu atoms into Mg–Si co-clusters can reduce the strain arising within the clusters due to the large difference in size between the Mg and Si atoms. Therefor, the driving force ΔG to evolve into energetically more preferable phases should be reduced in Cu containing clusters which in turn makes the clusters more thermally stable. The stabilizing effect of Cu-incorporation can result in a higher resilience to change and thus a more sluggish phase transformation. Clusters in the 6110 (0.094 at.% Cu) are therefore less affected by a ramp compared to the clusters from the 6082 (0.004 at.% Cu).

When looking into the precipitate CS distribution of the 6082 alloy, as seen in Fig. 6 (f), one sees a shift to smaller CS for the two ramped conditions, most notably for NA + rAA. Fig. 9 shows a HRTEM micrograph from the NA + rAA sample of this alloy in which the reason for this shift can be seen. Small precipitates some of which seem to be of the β"-type with four β"- eye molecules, sometimes referred to as $pre - \beta$" [33], coexist with more mature precipitates. The inset is a HAADF-STEM micrograph from the same condition of such an underdeveloped precipitate. The reason for the increased occurrence of such small precipitates after a ramp is not well understood. It could be related to the nucleation of new precipitates or to the dissolution of larger β"-type precipitates.

The DrAA treatment does, unlike the DAA treatment, introduce a certain amount of temperature lag or NA during which different kinds of cluster form. The samples' core temperature after 40 min ramping has only ~ 50 °C, see Fig. 1. That the ramp introduces some NA characteristics can also be seen in the conductivity curves from Fig. 4 (c) and (d) in which the curves of the DrAA treatment have a conductivity change which was qualitatively more comparable to the one of the NA + AA treatments. That clusters have formed during the ramp of the DrAA treatments becomes evident when comparing the hardness of the as-quenched condition with the condition right after the ramp, refer to Fig. 4 (a) and (b). An increase of hardness of ~ 20 HV can be measured while no visible traces of precipitates were found. Some of the clusters that form during the ramp might thus trap solute and vacancies or act as heterogeneous nucleation sites with the effect of a reduced precipitate number density. A reduced average precipitate number density for the DrAA heat treatments at peak strength is measured through TEM for both alloys, see Tables 3 and 4. This leads, thus, to more solute per precipitate, see also Tables 7 and 8. The available solute per precipitate is, due to the reduced precipitate number density, higher for the DrAA treatment. This gives individual precipitates in the DrAA treatment access to more free solute and enables the precipitates to grow quicker and longer, as will
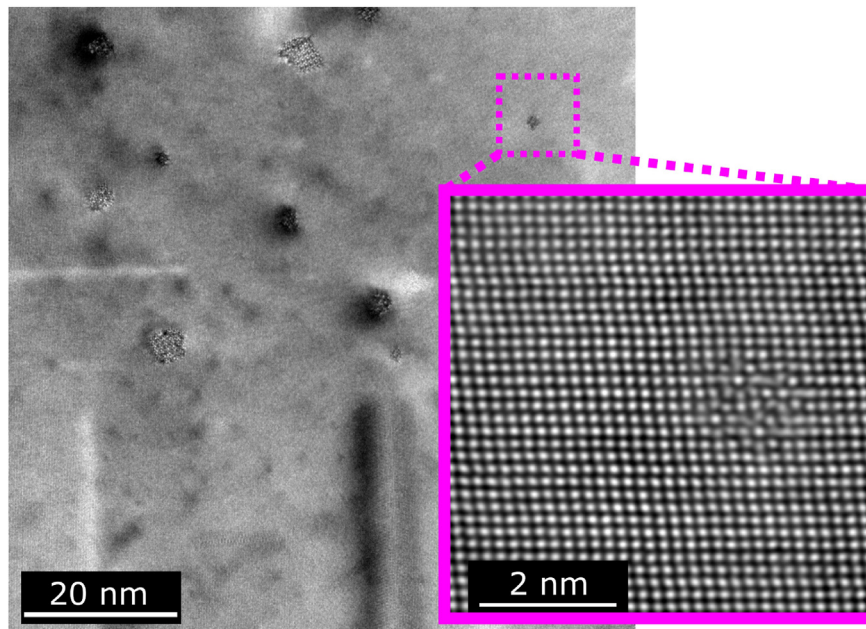
Fig. 9 – HRTEM and HAADF-STEM image of 6082 NA + rAA. The HRTEM image shows a mix of large and small precipitates where a few of them seem to contain only four β'' molecules. The inset shows one of those precipitates and is low pass filtered with a cut-off radius of $\sim 8\,nm^{-1}$.

be addressed later. The APT data shows after 10 h AA still a substantial difference of available free solute in the matrix for the DrAA treatment for 6110 compared to the DAA treatment, refer to Table 7. For 6082 this difference between the DAA and DrAA treatments were marginal, refer Table 8. The conductivity curves of Fig. 4 (c) and (d) show that the DrAA curves have a lower conductivity value compared to the DAA treatment during the first 24 h of AA. This difference is due to the explosive increase of the conductivity during the DAA treatment associated to the nucleation of a large number of small particles and ultimately a lower amount of solute left in solid solution [4,34]. Thus, the conductivity curves support the TEM and APT results.

The surplus of solute in the matrix around the precipitates explains the observed increased l_{mean} in the TEM data for the DrAA treatment when compared to the DAA treatment. The mean CS does not change substantially between the DAA and DrAA heat treatments. An increase of the CS is normally due to post-phases. The amount of post-phases is thus similar in the two heat treatments for both alloys which was also confirmed by high resolution HAADF-STEM, as seen in Table 5 and in Table 6.

4.3. Correlating hardness to the TEM and APT data

The DrAA treatments showed for both alloys a reduced average precipitate number density compared to the DAA treatments. The measured peak hardness of the DAA treatments were, however, still matched (6082) or even surpassed (6110). In the following section, we elaborate on these observations on the basis of the acquired TEM and APT data. At the end of this section we address the difference in the hardness kinetics and the reduced thermal stability of the ramped conditions.

4.3.1. Increased solid solution strengthening through reduced precipitate number density at peak hardness
The measured matrix compositions obtained for 6110 through APT analysis revealed a significant difference in the amount of Mg and Si remaining in matrix in DrAA which were about two and three times as large as for DAA. The degree of Cu depletion in the matrix was also higher for DAA compared to DrAA. For 6082, the amount of remaining solute of DAA and DrAA was comparable. The reason for the differences of solute in solid solution originates from the difference of the precipitate number density. In case of the 6082 alloy, for which the difference of solute in solid solution is minor yet has the same trend as in the 6110, the DrAA treatment resulted in a slightly decreased average precipitate number density, compared to the DAA treatment. In the case of the 6110 alloy the average precipitate number density is significantly decreased in the DrAA treatment compared to the DAA treatment, hence more solute can be found in solid solution. The difference of solute in solid solution and the reduced precipitate number density manifests itself in the lower conductivity of the DrAA treatments, compared to the DAA treatments, as earlier addressed.

The remaining Mg, Si and Cu in the matrix can provide a strengthening contribution through solid solution strengthening, $\Delta\sigma_{SS}$, typically added linearly with the intrinsic strength of pure aluminum and precipitate strengthening to estimate the overall yield strength. The contribution from solid solution can be expressed as [13]:

$$\Delta\sigma_{SS} = \sum_i k_i C_i^{\frac{2}{3}} \tag{2}$$

where the concentration in wt.%, C_i of each solute element i in solid solution is scaled by a specific scaling factor k_i and added linearly. The scaling factor of Mg, Si and Cu in Al are given in

Ref. [13] as 29.0, 66.3 and 46.4 $\frac{MPa}{wt.\%^{\frac{2}{3}}}$, respectively. Table 9 shows the resulting contributions of solid solution strengthening based on the solute amount found in matrix of the atom probe data of 6110 and 6082, DAA and DrAA.

It can be seen that the DrAA treatment for 6110 results in an increased contribution to strength from solid solution. For the 6082 no significant difference could be estimated. Even though the contribution of precipitation hardening dominates the strengthening effect of 6xxx, the contribution of solute solution strengthening can be an additional factor in explaining the increased hardness values for the DrAA treatment for the 6110.

4.3.2. Correlating precipitate statistics to the peak hardness

The overall strength is lower for the 6082 than for the Cu-rich 6110. This is due to the higher amount of evenly distributed precipitates in 6110, attributed to the larger amount of Cu [7]. The DrAA treatment for 6110 results in an increased peak hardness, compared to the DAA treatment. The main explanation for this behaviour can be seen in the precipitate microstructure:

Even though DrAA decreases the average precipitate number density significantly compared to DAA, the average precipitate length gets nearly doubled, see Table 3, which increases their effectiveness in interacting with dislocations. Nie et al. [35] showed that the aspect ratio of a given precipitate distribution has a significant influence on the critical resolved shear stress (CRSS). Longer precipitates can interact more frequently in materials of high stacking-fault energy, where cross-slipping is one of the main passing mechanisms [36]. This in return retards the dislocation movement more and results in better mechanical properties. A higher CRSS was shown to result for elongated precipitates over spherical precipitates already at an aspect ratio of two for different volume fractions [35]. The DrAA treatment of the 6082 does not result in higher hardness values than the DAA treatment, because the increase of l_{mean}, due to the ramp, does not increase the precipitate aspect ratio substantially, since the DAA treatment already produces fairly long precipitates, as seen in Table 4. However, the increase of l_{mean} by ~ 6 nm does still compensate for the decrease in ρ due to the ramp.

The precipitate CS and length distribution for both the DAA and DrAA samples are monomodal and narrow in both alloys, as seen in Fig. 5 (e), (f) and Fig. 6 (e), (f). Hence, the underlying formulas of the yield strength module from the NaMo model can directly be applied to compare the strengthening effect of the precipitates and to correlate and re-affirm the measured hardness values and precipitate statistics. For calculating the

strength contribution due to precipitates, we assume spherical precipitates and apply textbook equations to derive their strength contribution. Even though this assumption is wrong and more sophisticated models exist [37,38], it has been shown that the more sophisticated models produce a qualitatively similar outcome [39]. The microstructure can thus be related to the measured hardness values. For an in detail introduction to the NaMo model and the derivation of the formulas the reader is referred to Refs. [13,27]. The main precipitate found after 10 h AA at 175 °C is of the shearable β''-type, see Tables 5 and 8. The force F a shearable precipitate opposes to a gliding dislocation is given as:

$$F = 2\beta Gb^2 \frac{r_p}{r_c} \tag{3}$$

where G is the shear modulus of Al 26.5 GPa, b is the Burger's vector of Al, $b = 0.286$ nm, and $\frac{r_p}{r_c}$ being the ratio of the average mean precipitate radius r_p and the critical radius r_c. The constant β is 0.5. The value for the critical radius r_c was taken for 6110 from Ref. [27] and is $r_c = 4.5$ nm r_c describes the transition radius between particle shearing and bypassing. For 6082 we assumed that $r_c = 5.5$ nm. The precipitate radius r_p is given by:

$$r_p = \left(\frac{3V_p}{4\pi}\right)^{\frac{1}{3}} \tag{4}$$

The radius of a needle-shaped precipitate is therefore given by a sphere of the same precipitate volume as the average precipitate $V_p = l_{mean} \times CS$. The final increase in strength $\Delta\sigma_{shear}$ due to shearable precipitates can then be expressed as:

$$\Delta\sigma_{shear} = \frac{M}{b^2\sqrt{\beta G}}\sqrt{\rho r_p F^{\frac{3}{2}}} \tag{5}$$

with ρ being the number density and $M = 3$ is the Taylor factor. The values of the directly aged 6110 samples, taken from Table 3, yield a precipitates' strength contribution of 332 MPa for the DAA sample and 372 MPa for the DrAA one. The increased precipitate length compensates, thus, for the reduced precipitate number density and even increases the overall performance of the 6110. The ramped condition exhibits here a ~ 12% increase of strength due to longer precipitates. Shi et al. [31] measured a similar effect due to applying a ramp before AA. They measured a ~ 10% increase in strength when ramping a AA6061 cyclic strengthened sample slowly up to AA temperature relative to no ramp.

Applying the equations to the 6082 alloy with the values from Table 4, a contribution of strength due to precipitates of 307 MPa for the DAA sample and 312 MPa for the DrAA sample can be estimated. This corresponds well with the measured hardness values from Fig. 4 (b) which are nearly equal after 10 h AA for these two treatments.

4.3.3. Discussing the changed hardening kinetics and the difference in thermal stability

The four heat treatments for the 6110 have different hardening kinetics, as can be seen in Fig. 4 (a). The DAA treatment surpasses 100 HV after roughly 20 min, the DrAA treatment after ~ 50 min and the NA + AA and NA + rAA treatments after around 100 min of AA. This behaviour is explained through

Table 9 – Contribution of solid solution strengthening from the three main solutes: Mg, Si and Cu. The values are given in MPa and the accumulated contribution to strength $\Delta\sigma_{SS}$ in the last row.

MPa	6110		6082	
	DAA	DrAA	DAA	DrAA
σ_{Mg}	6.5	12.7	1.7	1.8
σ_{Si}	5.5	20.4	11.2	11.3
σ_{Cu}	10.8	9.3	–	–
$\Delta\sigma_{SS}$	22.8	42.5	12.9	13.1

the influence of a ramp on quenching clusters and the detrimental effect of NA clusters and their retrogression. In underaged conditions it can be assumed that the microstructure of 6xxx alloys contains a high density of small, nearly equiaxed precipitates [40,41]. The strength contribution of cutting such finely dispersed, small particles is estimated through $\Delta\sigma_{shear} \sim \sqrt{\rho}$. As the AA proceeds, some of those precipitates will grow while others dissolve, resulting in precipitates of a distinct needle-like morphology and a decreased precipitate number density. Due to the effect of a ramp on the quenching clusters, the number density of precipitates is lower in the underaged condition of the DrAA treatment. Therefore the hardening response is delayed. This is supported by the measured strong increase in conductivity after 20 min AA during the DAA treatment compared to the DrAA treatment, see Fig. 4 (c). The retrogression which takes place at the beginning of the isothermal AA treatment delays the hardening response of the NA + AA and NA + rAA treatments and results in a drastic reduction of the number density of precipitates. This is confirmed by the average precipitate number densities acquired through TEM at peak age, as shown in 3.

The four heat treatments of the 6082 do not show a difference in hardening kinetics, as seen in Fig. 4 (b). In this alloy, the DAA and DrAA as well as NA + AA and NA + rAA show pairwise similar hardening evolution. The hardening response of the NA + AA and NA + rAA conditions is delayed due to retrogression, as well. Even though a difference in the number density of small precipitates between the DAA and DrAA treatment must be assumed, a similar change of hardness appears. The reason for this is that both heat treatments produce a precipitate number density which is roughly of the same order for magnitude. The same reasoning explains the similarity of hardness evolution in the NA + AA and NA + rAA treatment for 6082 and 6110.Both alloys show a shorter hardness plateau when ramped, regardless of the amount of NA. This becomes especially apparent for the 6082 alloy in which a double-peak aging behavior can be seen. The ramped samples show a lower amount of overaged precipitates and more of the early precipitates which might partly explain their reduced thermal resistance. However, the origin of the double peak and thus the higher thermal stability for the not ramped samples is not fully understood and currently under investigation.

4.4. Influence of the heat treatment on the precipitates

4.4.1. Changed precipitate type
The precipitate type analysis from Tables 5 and 6 shows a general trend from ramping up to AA: an increased amount of $\beta''_{perfect}$ on the expense of β''_{Hybrid} and less of the later metastable phases, e.g. Q'/B'. The β''_{Hybrid}-precipitates show a large continuous region of the β''-molecules alongside structural components of some phases that appear later in the precipitation sequence, as shown in Figs. 7 and 8. More of the overaged B' type precipitates are found in the 6082 when not ramped and more of the L/C type precipitates —typically found together with β'' in the

precipitation sequence [5,8]— are found in the Cu-rich 6110, when ramped. Another indication for more overaged phases when not ramped can be found by comparing the average CS. Overaged phases typically have a larger CS [40]. That the precipitates have larger CS when not ramped becomes especially notable when comparing the average CS and the CS distributions for the 6082 ramped vs. not ramped, see Table 4 and Fig. 6 (f).

An explanation for the apparent increased occurrence of structures from typical overaged phases, e.g. Q'/B', U2, in the DAA and NA + AA treatments is, that an excess energy input $\frac{\delta T}{\delta t}$, by introducing the alloys into pre-heated furnance, during the crucial stage of precipitate formation and early growth, facilitates the growth and formation of atomic structures of phases from later stages of the precipitation sequence early on. On the contrary, a limited energy input, e.g. a ramp, forces the system to follow the precipitation sequence more strictly to successively lowering its free enthalpy. Hence, we see an increased amount of $\beta''_{perfect}$ and L/C phases during the DrAA and NA + rAA treatments which appear early on in the precipitation sequence. In the case of the 6110 DAA treatment an increase of overaged structures could also be attributed due to the condition being closer situated to the end of the hardening plateau, due to a difference in hardening kinetics as discussed earlier. This could have lead to an increased occurrence of hybrid and overaged structures. However, an increased occurrence of overaged structures was seen in both alloys and all analyzed conditions which were heat treated without a ramp.

4.4.2. Changed precipitate length
Another trend which was observed in both alloys is, that the DrAA treatments result in a longer average precipitate length than in the DAA treatments, see Tables 3 and 4. This becomes especially apparent in the 6110 alloy where the length nearly doubles. The reason for the increased precipitate length could be explained, for the 6110, through the higher amount of L phases, which are known to possess large aspect ratios [9]. This would, however, not explain the increased length in the DrAA 6082. Another explanation for the increased length due to a ramp can be found in the occurrence of more pure $\beta''_{perfect}$. The large aspect-ratio of needle shaped β'' precipitates is mainly dictated by the anisotropic interface energy between precipitate and matrix and to some extend by the elastic anisotropy of the parental fcc-Al and the monoclinic precipitate [42]. An increased interface energy of β''_{Hybrid} phases compared to $\beta''_{perfect}$ can be assumed due to the presence of overaged and therefore less coherent parts in β''_{Hybrid}. Hence, the β''_{Hybrid} precipitates can be expected to grow slower due to larger interface energies, resulting ultimately in shorter precipitate lengths.

As already addressed earlier, the APT measurements detected an increased amount of solute left between the precipitates for the DrAA treatment compared to the DAA treatment, especially pronounced for the 6110 alloy. This correlates well to the strongly reduced measured average precipitate number density encountered in the DrAA treatment. As an result, more solute is left per precipitate and the higher solute concentration in the

matrix would allow the precipitates to grow faster. The $\beta''_{perfect}$ precipitates are coherently embedded within the Al matrix along their sides, having, however, incoherent end parts. Incoherent interfaces are known for having a higher mobility, thus advancing faster than coherent interfaces and resulting in the needle-like morphology [43]. The higher solute concentration in the matrix together with the precipitate growth behaviour can thus result in an increased average precipitate length for the precipitates of the DrAA treatments.

5.   Conclusion and summary

This work studies two different Al–Mg–Si(-Cu) alloys and shows that ramping to AA temperature leads to significant changes in the microstructure compared to directly bringing the samples to the AA temperature. It is found that direct heating without a ramp (DAA and NA + AA), leads to more structural components of overaged phases and a changed average precipitate number density at peak hardness. A ramp to AA temperature leads to longer precipitates, more of the purer $\beta''_{perfect}$ phases and less overaged ones, e.g. B'. This influences the overall hardening behavior:

- The Ramping of 6082 and 6110 directly from a SSSS results in a reduced average precipitate number density compared to no ramp. As a consequence more solute is left in solid solution at peak hardness when ramped and precipitates grow longer.
- Directly ramping the 6110 and 6082 up to artificial aging temperature increases the l_{mean} and thus the aspect ratio of the average precipitate compared to no ramp. This leads, in the 6110, to an increased peak strength.
- Ramping the 6110 and 6082 leads to a shorter strength plateau.

Both alloys respond to a ramp after 28 days of NA with an increased average precipitate number density compared to no ramp. However, the still unknown nature of the clusters that emerge during NA in the 6xxx system impede that a complete understanding of the clustering which happens during a ramp can be achieved. It was, however, shown that the heating rate to AA temperature is a parameter which is worthy to explore in further works.

Data availability

The raw/processed data required to reproduce these findings cannot be shared at this time as the data also forms part of an ongoing study.

Declaration of Competing Interest

The authors declare that they have no known competing financial interests or personal relationships that could have appeared to influence the work reported in this paper.

REFERENCES

[1] Schatzberg E. Symbolic culture and technological change : the cultural history of aluminum as an industrial material. February. 2015. p. 226–71. https://doi.org/10.1017/S1467222700012234.

[2] Kelly A, Nicholson RB. Precipitation hardening. Denki-Seiko [Electric Furnace Steel] 1966;37(2):65–72. https://doi.org/10.4262/denkiseiko.37.65. 86.

[3] Roesler J, Harders H, Baeker M. Mechanical behaviour of engineering Materials_Metals, ceramics, polymers, and composites. 2007.

[4] P. Dumitraschkewitz, S. S. Gerstl, L. T. Stephenson, P. J. Uggowitzer, S. Pogatscher, Clustering in age-hardenable aluminum alloys, Adv Eng Mater 20 (10). doi:10.1002/adem.201800255..

[5] Saito T, Mørtsell EA, Wenner S, Marioara CD, Andersen SJ, Friis J, Matsuda K, Holmestad R. Atomic structures of precipitates in Al–Mg–Si alloys with small additions of other elements. jul. 2018. https://doi.org/10.1002/adem.201800125. URL, http://doi.wiley.com/10.1002/adem.201800125.

[6] R. Holmestad, C. D. Marioara, F. J. H. Ehlers, M. Torsaeter, R. Bjørge, J. Røyset, S. J. Andersen, Precipitation in 6xxx aluminum alloys.

[7] Marioara CD, Andersen SJ, Stene TN, Hasting H, Walmsley J, Van Helvoort AT, Holmestad R. The effect of Cu on precipitation in Al-Mg-Si alloys. Phil Mag 2007;87(23):3385–413. https://doi.org/10.1080/14786430701287377.

[8] Jia Z, Ding L, Cao L, Sanders R, Li S, Liu Q. The influence of composition on the clustering and precipitation behavior of Al-Mg-Si-Cu alloys. Metall Mater Trans A 2017;48(1):459–73. https://doi.org/10.1007/s11661-016-3850-7.

[9] Sunde JK, Marioara CD, Holmestad R. The effect of low Cu additions on precipitate crystal structures in overaged Al-Mg-Si(-Cu) alloys. Mater Char 2020;160(November 2019):110087. https://doi.org/10.1016/j.matchar.2019.110087. URL https://doi.org/10.1016/j.matchar.2019.110087.

[10] B. Milkereit, M. J. Starink, P. A. Rometsch, C. Schick, O. Kessler, Review of the quench sensitivity of aluminium alloys: analysis of the kinetics and nature of quench-induced precipitation, Materials 12 (24). doi:10.3390/MA12244083..

[11] Werinos M, Antrekowitsch H, Ebner T, Prillhofer R, Uggowitzer PJ, Pogatscher S. Hardening of Al-Mg-Si alloys: effect of trace elements and prolonged natural aging. Mater Des 2016;107:257–68. https://doi.org/10.1016/j.matdes.2016.06.014. URL https://doi.org/10.1016/j.matdes.2016.06.014.

[12] Banhart J, Chang CST, Liang Z, Wanderka N, Lay MDH, Hill AJ. Natural aging in Al-Mg-Si alloys - a process of unexpected

complexity. Adv Eng Mater 2010;12(7):559—71. https://doi.org/10.1002/adem.201000041. URL http://doi.wiley.com/10.1002/adem.201000041.

[13] Myhr OR, Grong Ø, Schäfer C. An extended age-hardening model for Al-Mg-Si alloys incorporating the room-temperature storage and cold deformation process stages. Metall Mater Trans A 2015;46(12):6018—39. https://doi.org/10.1007/s11661-015-3175-y.

[14] Andersen SJ. Quantification of the Mg2Si β'' and β' phases in AlMgSi alloys by transmission electron microscopy. Metall Mater Trans 1995;26(8):1931—7. https://doi.org/10.1007/BF02670664.

[15] Kelly PM, Jostsons A, Blake RG, Napier JG. The determination of foil thickness by scanning transmission electron microscopy. Phys Status Solidi 1975;31(2):771—80. https://doi.org/10.1002/pssa.2210310251.

[16] D. J. Larson, T. Prosa, R. M. Ulfig, B. P. Geiser, T. F. Kelly, Local electrode atom probe tomography, New York, US: Springer Science 2..

[17] Hatzoglou C, Radiguet B, Pareige P. Experimental artefacts occurring during atom probe tomography analysis of oxide nanoparticles in metallic matrix: quantification and correction. J Nucl Mater 2017;492:279—91.

[18] De Geuser F, Lefebvre W, Blavette D. 3d atom probe study of solute atoms clustering during natural ageing and pre-ageing of an al-mg-si alloy. Phil Mag Lett 2006;86:227—34. 04.

[19] Esmaeili S, Vaumousse D, Zandbergen M, Poole W, Cerezo A, Lloyd D. A study on the early-stage decomposition in the al—mg—si—cu alloy aa6111 by electrical resistivity and three-dimensional atom probe. Phil Mag 2007;87(25):3797—816.

[20] Wenner S, Lervik A, Thronsen E, Marioara CD, Kubowicz S, Holmestad R. Copper enrichment on aluminium surfaces after electropolishing and its effect on electron imaging and diffraction. Mater Char 2021;172:110846.

[21] Danoix F, Miller M, Bigot A. Analysis conditions of an industrial al—mg—si alloy by conventional and 3d atom probes. Ultramicroscopy 2001;89(1—3):177—88.

[22] Esmaeili S, Lloyd DJ. Effect of composition on clustering reactions in AlMgSi(Cu) alloys. Scripta Mater 2004;50(1):155—8. https://doi.org/10.1016/j.scriptamat.2003.08.030.

[23] L. Ding, Z. Jia, Z. Zhang, R. E. Sanders, Q. Liu, G. Yang, The natural aging and precipitation hardening behaviour of Al-Mg-Si-Cu alloys with different Mg/Si ratios and Cu additions, Mater Sci Eng 627 (2015) 119—126. doi:10.1016/j.msea.2014.12.086. URL https://doi.org/10.1016/j.msea.2014.12.086.

[24] M. Torsæter, H. S. Hasting, W. Lefebvre, C. D. Marioara, J. C. Walmsley, S. J. Andersen, R. Holmestad, The influence of composition and natural aging on clustering during preaging in Al-Mg-Si alloys, J Appl Phys 108 (7). doi:10.1063/1.3481090..

[25] Edwards GA, Stiller K, Dunlop GL, Couper MJ. The precipitation sequence in Al-Mg-Si alloys. Acta Mater 1998;46(11):3893—904. https://doi.org/10.1016/S1359-6454(98)00059-7.

[26] Peng J, Bahl S, Shyam A, Haynes JA, Shin D. Solute-vacancy clustering in aluminum. Acta Mater 2020;196:747—58. https://doi.org/10.1016/j.actamat.2020.06.062.

[27] Engler O, Marioara CD, Aruga Y, Kozuka M, Myhr OR. Effect of natural ageing or pre-ageing on the evolution of precipitate structure and strength during age hardening of Al—Mg—Si alloy AA 6016. Mater Sci Eng 2019;759(May):520—9. https://doi.org/10.1016/j.msea.2019.05.073. U RL https://doi.org/10.1016/j.msea.2019.05.073.

[28] Pogatscher S, Antrekowitsch H, Leitner H, Ebner T, Uggowitzer PJ. Mechanisms controlling the artificial aging of Al-Mg-Si Alloys. Acta Mater 2011;59(9):3352—63. https://doi.org/10.1016/j.actamat.2011.02.010. UR L https://doi.org/10.1016/j.actamat.2011.02.010.

[29] Pogatscher S, Werinos M, Antrekowitsch H, Uggowitzer PJ. The role of vacancies in the aging of Al-Mg-Si alloys. Mater Sci Forum 2014;794—796:1008—13. https://doi.org/10.4028/www.scientific.net/MSF.794-796.1008.

[30] Tao GH, Liu CH, Chen JH, Lai YX, Ma PP, Liu LM. The influence of Mg/Si ratio on the negative natural aging effect in Al-Mg-Si-Cu alloys. Mater Sci Eng 2015;642:241—8. https://doi.org/10.1016/j.msea.2015.06.090.

[31] Shi L, Baker K, Young R, Kang J, Liang J, Shalchi-Amirkhiz B, Langelier B, Brechet Y, Hutchinson C, Zurob H. The effect of chemical patterning induced by cyclic plasticity on the formation of precipitates during aging of an Al—Mg—Si alloy. Mater Sci Eng 2021;815(February):141265. https://doi.org/10.1016/j.msea.2021.141265. UR L https://doi.org/10.1016/j.msea.2021.141265.

[32] Zandbergen MW, Cerezo A, Smith GD. Study of precipitation in Al-Mg-Si Alloys by atom probe tomography II. Influence of Cu additions. Acta Mater 2015;101:149—58. https://doi.org/10.1016/j.actamat.2015.08.018. UR L https://doi.org/10.1016/j.actamat.2015.08.018.

[33] Marioara CD, Andersen SJ, Jansen J, Zandbergen HW. Atomic model for GP-zones in a 6082 Al-Mg-Si system. Acta Mater 2001;49(2):321—8. https://doi.org/10.1016/S1359-6454(00)00302-5.

[34] Bahrami A, Yazdan Mehr M. Modeling electrical resistivity of naturally aged al—mg—si alloys. Metals 2019;9(3):310.

[35] Nie JF, Muddle BC, Polmear IJ. The effect of precipitate shape and orientation on dispersion strengthening in high strength aluminium alloys. Mater Sci Forum 1996;217—222(PART 2):1257—62. https://doi.org/10.4028/www.scientific.net/msf.217-222.1257.

[36] Hazif RL, Poirier J-P. Cross-Slip on (100) planes in aluminum single crystals compressed along (100) axis. Acta Metall 1975;23(7):865—71.

[37] Holmedal B. Strength contributions from precipitates. Phil Mag Lett 2015;95(12):594—601.

[38] Bahrami A, Miroux A, Sietsma J. An age-hardening model for al-mg-si alloys considering needle-shaped precipitates. Metall Mater Trans 2012;43(11):4445—53.

[39] Gulbrandsen-Dahl S, Marioara CD, Pedersen KO, Marthinsen K. Hardening of Al-Mg-Si alloys and effect of particle structure. Mater Sci Forum 2012;706—709(2):283—8. https://doi.org/10.4028/www.scientific.net/MSF.706-709.283.

[40] Sunde JK, Lu F, Marioara CD, Holmedal B, Holmestad R. Linking mechanical properties to precipitate microstructure in three Al-Mg-Si(-Cu) alloys. Mater Sci Eng October 2020;807. https://doi.org/10.1016/j.msea.2021.140862.

[41] Nie JF, Muddle BC. Microstructural design of high-strength aluminum alloys. J Phase Equil 1998;19(6):543—51. https://doi.org/10.1361/105497198770341734.

[42] H. Mao, Y. Kong, D. Cai, M. Yang, Y. Peng, Y. Zeng, G. Zhang, X. Shuai, Q. Huang, K. Li, H. Zapolsky, Y. Du, β'' needle-shape precipitate formation in Al-Mg-Si alloy: phase field simulation and experimental verification, Comput Mater Sci 184 (June). doi:10.1016/j.commatsci.2020.109878.

[43] Porter D, Easterling K, Sherif MY. Phase transformations in metals and alloys. 2009.